Journal of Marine Systems 252 (2025) 104143

Contents lists available at ScienceDirect

Journal of Marine Systems

journal homepage: www.elsevier.com/locate/jmarsys

Lagrangian dispersion in the Red River plume region, Northeast Vietnam, from drifter observations and modeling

Alexei Sentchev [a,f,*], Thinh Nguyen-Duc [b], Stefano Berti [c], Nadia K. Ayoub [d,f], Vu Duy Vinh [e]

[a] Laboratory of Oceanology and Geosciences, UMR8187, Univ. Littoral Côte d'Opale, CNRS, Univ. Lille, IRD, F-62930 Wimereux, France
[b] Institute of Oceanography, Vietnam Academy of Science and Technology (VAST), Nha Trang, Viet Nam
[c] Univ. Lille, ULR 7512, Unité de Mécanique de Lille Joseph Boussinesq (UML), F-59000 Lille, France
[d] University of Toulouse, LEGOS (CNRS, IRD, CNES, UPS), F-31401 Toulouse, France
[e] Institute of Scence and Technology for Energy and Environment (ISTEE), Vietnam Academy of Science and Technology (VAST), Haiphong, Viet Nam
[f] LMI LOTUS, Univ. Sci. Tech. of Hanoi, Hanoi, Viet Nam

ARTICLE INFO

Keywords:
Lagrangian dispersion
River plume
Relative dispersion
Surface drifters
SYMPHONIE model
The Red River

ABSTRACT

The transport and spatial distribution of materials within river plumes and neighboring waters are strongly influenced by the plume morphology and fronts bounding the plume area. Thus, identifying locations of plume fronts and assessing frontal mixing activity is particularly important for understanding the spatial distribution of biogeochemical tracers and the connectivity between source (river mouth) and offshore regions. Statistical properties of horizontal dispersion in the Red River (RR) plume region were obtained from drifter experiments, conducted in the Gulf of Tonkin during summer 2022, and also from realistic numerical modeling. Adopting a Lagrangian perspective, a method is proposed to characterize the RR plume morphology based on the extraction of Lagrangian Coherent Structures (LCS) from the surface flow field using Finite-Size Lyapunov Exponents (FSLE). Maxima of the attracting FSLE field (FSLE ridge lines) enabled us to identify zones of current convergence and shear in the flow, which are essential for characterizing the dynamics associated with plumes and mapping the fronts delimiting them. It became clear that the body of the RR plume is formed by the individual river plumes of the RR deltaic system. FSLE ridge lines allowed identification of the offshore expansion of individual plumes and revealed a variety of forms, semi-circular or hook-like filaments, characterizing the plume shape. The ballistic regime of dispersion was found inside the plume region, with the dominant direction perpendicular to the coastal flow direction revealing anisotropic shear dispersion. It was observed at scales of 0.3 to 3 km (submesoscale range), with a maximum value of 10–13 day^{-1}, as derived from the analysis of the scale dependent relative dispersion of real drifters. In model simulations, the relative dispersion appeared scale independent in the range below 2 km, indicating a significant effect of grid resolution on the model's representation of lateral mixing.

1. Introduction

Transition zones where the freshwater released from a river mouth meets and interacts with a larger body of sea or ocean water are known as river plumes. The freshwater input creates a distinct, low-density layer that can extend outwards from the river mouth for tens of kilometers, in the case of large rivers such as the Columbia (Jay et al., 2010), the Connecticut (Cole et al., 2020), or hundreds of kilometers, in the case of the world's largest river systems such as the Amazon or the Mississippi (e.g., da Silva and Castelao, 2018; Coles et al., 2013). River plumes influence local salinity, temperature, and nutrient distribution (Kubryakov et al., 2016; da Silva and Castelao, 2018; Morozov et al., 2024). Therefore, river plumes have a significant impact on coastal ecosystems, marine life and water quality, transporting sediments and nutrients that support biological productivity (e.g., Dagg et al., 2004; Han et al., 2012; Moline et al., 2008).

The structure of river plumes, the transport and mixing of river and sea water have been the subject of extensive studies, as described in several research reviews (O'Donnell, 2010; Hetland and Hsu, 2013; Horner-Devine et al., 2015). Particular attention was paid to characterizing the main plume front, a region featuring strong convergence of surface flow, downwelling, and enhanced mixing (e.g., Jay et al., 2009;

* Corresponding author at: Laboratory of Oceanology and Geosciences, UMR8187, Univ. Littoral Côte d'Opale, CNRS, Univ. Lille, IRD, F-62930 Wimereux, France.
E-mail address: alexei.sentchev@univ-littoral.fr (A. Sentchev).

https://doi.org/10.1016/j.jmarsys.2025.104143
Received 22 January 2025; Received in revised form 19 August 2025; Accepted 29 September 2025
Available online 2 October 2025

O'Donnell et al., 1998; Marmorino and Trump, 2000; Orton and Jay, 2005).

Many recent studies have shown that numerical coastal circulation models have proved capable of quantifying plume behavior in different geographic regions. Realistic numerical simulations of the circulation in the Long Island Sound (the Connecticut river plume), have demonstrated that in coastal environments, characterized by energetic tidal motions, the combination of tidally pulsed outflows through the mouth and rapid tidal currents can cut off plume waters from their source and create a series of discrete plume pulses (e.g., Whitney et al., 2021). This recurrent phenomenon can generate multiple frontal zones over a wide plume region. Similar results were obtained in the Merrimack River plume (e.g., Cole et al., 2020), the Columbia River plume (e.g., Horner-Devine et al., 2009; Nash et al., 2009), both located in a much lower-energy tidal environment. Observations and numerical simulations have clearly demonstrated the decisive effect of tides on plume morphology. The role of tides in shaping the Gironde river plume in the Bay of Biscay, as well as in generating the recirculation gyres at the estuary outlet and a bulge, has been characterized by Toublanc et al. (2023). Besides, baroclinic and barotropic instabilities at the Gironde river plume fronts were obtained in response to variations mainly in wind and freshwater discharge (Ayouche et al., 2021).

These and some other recent studies have demonstrated that numerical modeling can be a highly effective tool, offering the possibility to study the impact of each individual forcing and also of the whole plume dynamics. However, significant gaps still exist in our knowledge of the effects of winds, or of frontal mixing on plume evolution. Perhaps more importantly, the physical mechanisms that control the plume horizontal expansion, assumed to be known, are not well reproduced in the models. Understanding the circulation patterns near the plume edge and the dominant mixing mechanisms at the plume fronts remains a challenge.

The transport and dispersion of pollutants, sediments, and biological materials are strongly influenced by plume morphology and its bounding fronts (Warrick and Farnsworth, 2017; Yankovsky et al., 2022; Bertin et al., 2024). Identifying plume fronts and assessing frontal mixing are therefore crucial for understanding the spatial distribution of biogeochemical materials and the connectivity between the river mouth and offshore regions as highlighted in earlier studies (e.g., Cole et al., 2020; Whitney et al., 2021).

The definition of plume spatial extent varies among studies. Satellite observations of sea surface temperature, salinity, and ocean color (e.g., SeaWiFS, SMAP, Sentinel-2, Terra/Aqua) have been widely used to identify the extent of river plumes (D'Sa et al., 2007; Schroeder et al., 2012; Brando et al., 2015; Chen et al., 2017). However, their strong dependence on cloud-free conditions and limited revisit times hinders continuous monitoring. Therefore, a combination of realistic numerical model simulations and in-situ measurements, supported by remote sensing remains probably the most effective method of investigation.

The simplest method, applied directly to model outputs, uses a fixed surface salinity value or salinity-anomaly threshold to define plume boundaries. Nevertheless, this approach is highly site dependent (e.g., MacCready et al., 2009; Warrick and Farnsworth, 2017). Alternatively, passive tracer concentrations above a set threshold are often used to determine near-edge plume boundaries (e.g., Whitney et al., 2021; Nguyen-Duy et al., 2021). Both methods enable direct comparison of in situ observations (e.g., salinity or tracer concentrations from transect surveys) with their model counterparts. However, strong variability in current velocities, driven by wind, tides, and river runoff, together with enhanced turbulence and stirring, characterizes the outer boundaries of the plume. These processes, which are difficult for numerical models to reproduce, significantly affect the spatial distribution of tracers and, consequently, the plume shape, as demonstrated in the recent modeling investigation of the Red River plume by Nguyen-Duy et al. (2021).

Our study focuses on characterizing the expansion of the Red River (RR) plume during a high-flow summer season (June 2022) and the mechanisms governing this expansion. The RR is one of the largest rivers in Southeast Asia (Dai and Trenberth, 2002) and supplies about 60 % of the freshwater input to the Gulf of Tonkin (GoT) (e.g., Nguyen-Duy et al., 2021). Despite its importance as a source of freshwater, sediments, and nutrients to the GoT, few studies have investigated the dynamics of the RR plume.

Using multi-year simulations by the high resolution numerical model SYMPHONIE, Nguyen-Duy et al. (2021) extensively assessed the seasonal variability of the RR plume. The plume expansion was identified by mapping concentrations of tracers, similar to dye, released within the estuaries of the RR system under seasonally varying wind conditions and river discharge. The authors characterized the plume shape and offshore expansion for four representative periods identified through clustering analysis. For mean June conditions (represented by cluster 3), RR plume waters extended 30–60 km offshore and reached the 20 m or 40 m isobaths, depending on tracer concentration (10 % or 5 %, respectively). An even larger offshore expansion, up to 100 km for mean June conditions, was reported by Rogowski et al. (2019), who used salinity as a tracer of the RR plume. Another tracer used by Rogowski et al. (2019) was CDOM concentration, derived from the space-borne radiometry sensor MODIS, which has a coarse spatial resolution (9 km). Although this approach provided different estimates of the RR plume extent, it proved useful for assessing temporal variability.

These examples clearly demonstrate how strongly the choice of method or tracer can influence the assessment. Moreover, the use of passive soluble tracers is sensitive to the parameters applied in solving the transport equation, as well as to model grid size and velocity. The threshold tracer concentration used to delimit plume expansion may vary by a factor of two between studies as discussed in (Nguyen-Duy et al., 2021), leading to different plume patterns. At present, there is no universal or widely recognized method regarding the choice of tracers and methodologies for mapping river plumes.

In the present study, we propose a new method for characterizing river plume expansion that avoids the drawbacks mentioned above. Instead of solving the transport equation for tracers, our approach relies on the hypothesis that dynamical structures of the coastal flow field, particularly current convergence zones, define the plume boundaries and attribute a complex frontal structure to the river plume body. These dynamical structures, known as Lagrangian Coherent Structures (LCS), are identified within a Lagrangian framework by tracking neutrally buoyant particles in the model velocity field and estimating Finite-Size Lyapunov Exponents (FSLE). Maxima of the FSLE field, corresponding to ridge lines, allow us to detect zones of current convergence and enhanced shear in the flow, which are essential for characterizing plume morphology and mapping the fronts that delimit plumes.

Therefore, the main objectives of this study are the following: (1) determine the morphology and spatial expansion of the RR plume during the high-flow summer season using a Lagrangian framework, and (2) quantify Lagrangian dispersion across the plume region. To achieve these objectives, an approach combining high-resolution numerical modeling and surface drifter observations is taken. The morphology of the RR plume, as described in the study, provides context for the subsequent analysis of recently obtained observations in this region and establishes a basis for further investigations. From a practical perspective, characterizing transport and dispersion processes in the RR plume region addresses a major challenge for future monitoring of particulate matter fate in this part of the GoT, which hosts Vietnam's most famous tourist and economic sites.

2. Materials and methods

2.1. Study site and environmental conditions

The study region is located in the northwestern Gulf of Tonkin (Fig. 1a), a shallow water gulf, 450 km long and 270 km wide, which is a part of the East Sea in Southeast Asia. The gulf exchanges waters with

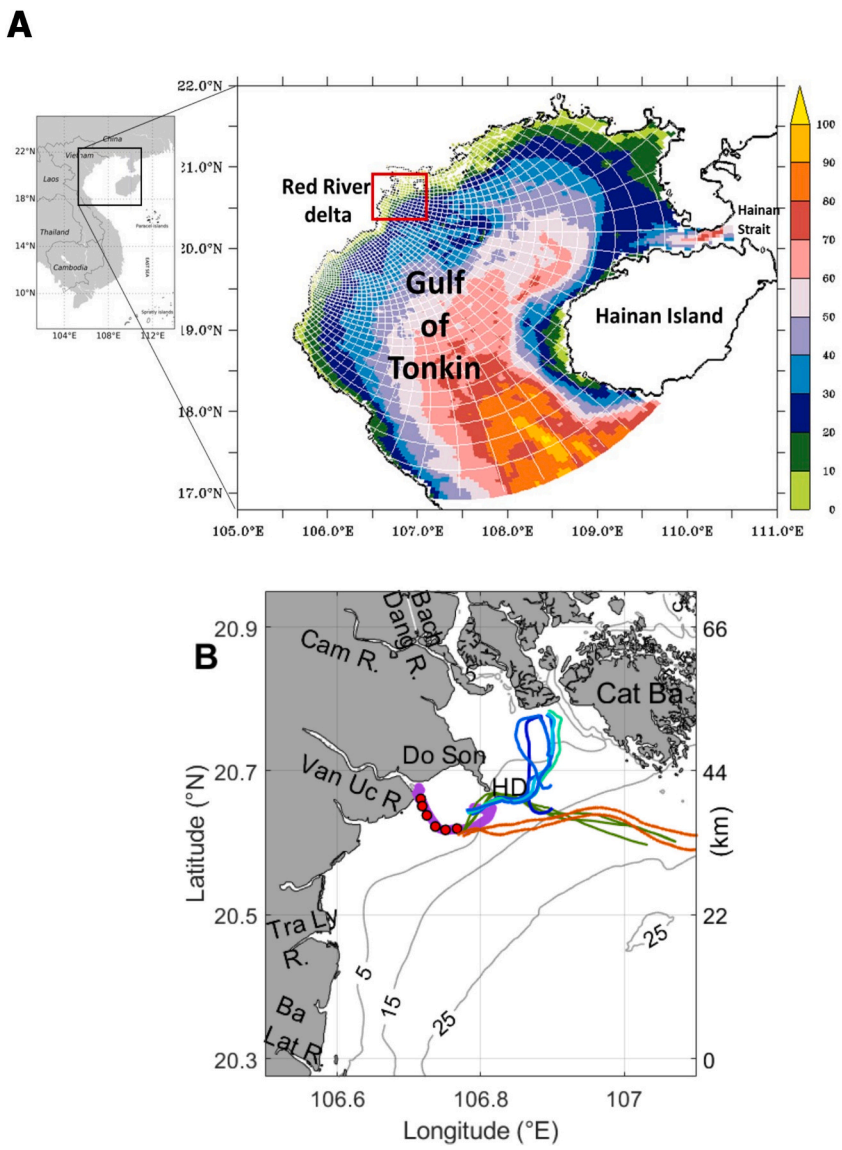

Fig. 1. (A) Gulf of Tonkin, its bathymetry in meters (color shading), and the curvilinear numerical grid used in the SYMPHONIE model simulations (white contours, only one of ten contours is shown). The red rectangle shows the location of the study region. (B) Study region and its bathymetry (in meters, grey contours). Surface buoy trajectories are shown by thick color lines. The large magenta line indicates the location of the towed ADCP transect, and red dotes mark the locations of CTD profiles along the transect. Geographic names mentioned in the text are also shown. "HD" denotes Hon Dau Island. (For interpretation of the references to color in this figure legend, the reader is referred to the web version of this article.)

the tropical Pacific ocean mainly through the large southern entrance and partly through the Hainan (or Qiongzhou) Strait in the east, which is quite deep (~50 m). The bathymetry of the gulf gradually increases from a few meters in the deltaic part, near the Vietnamese coast, to about 70 m in the southern part (Fig. 1a).

The study site, shown in Fig. 1b, has a complex coastline with numerous headlands and embayments, especially near the Red River (RR) delta. There are also many small islands, scattered along the RR delta, as well as the bigger Cat Ba Island. Water depth gradually increases from 5 m near the shore to 30 m at the southern and eastern boundaries of the site (Fig. 1b). The site receives freshwater from five of the six branches of the Red River, from south to north: the Ba Lat, the Tra Ly, the Van Uc, the Cam, and the Bach Dang rivers, which all contribute to a buoyant current along the Vietnamese coast. The Red River is the major source of freshwater in the gulf. Its mean discharge is about 4000 m^3s^{-1}, the range of seasonal variation is very large, from 2000 m^3s^{-1} to 12,000 m^3s^{-1}, during the rainy season, and it carries out a large volume of sediments (Vinh et al., 2014).

The RR plume dynamics is controlled by buoyancy input, winds, and tides. The changes in the balance between stratification and mixing occur on different time scales: from seasonal to monthly and from fortnightly down to one day or shorter (e.g., Nguyen-Duy et al., 2021; Tran et al., 2021). The seasonal variability is more prominent, as the plume is located in the tropical region, and hence affected by monsoonal cycles, and the freshwater discharge is the largest during the wet summer. In winter, the buoyant flow leaves the gulf as a trapped coastal current and joins a rectified tidal current in central Vietnam. In summer, under the influence of southwesterly monsoon winds, the river plume spreads further seaward (Nguyen-Duy et al., 2021; Rogowski et al., 2019).

An oceanographic campaign was organized in June 2022 to collect data on currents, temperature, salinity and turbidity profiles, as well as water samples for further analysis of the ecological state in this part of the GoT. The tidal range during the study period was close to 3 m (Fig. 2c), indicating spring tide conditions. The tidal gauge station is located on Hon Dau Island, 1 km southeast of the extremity of the Do Son

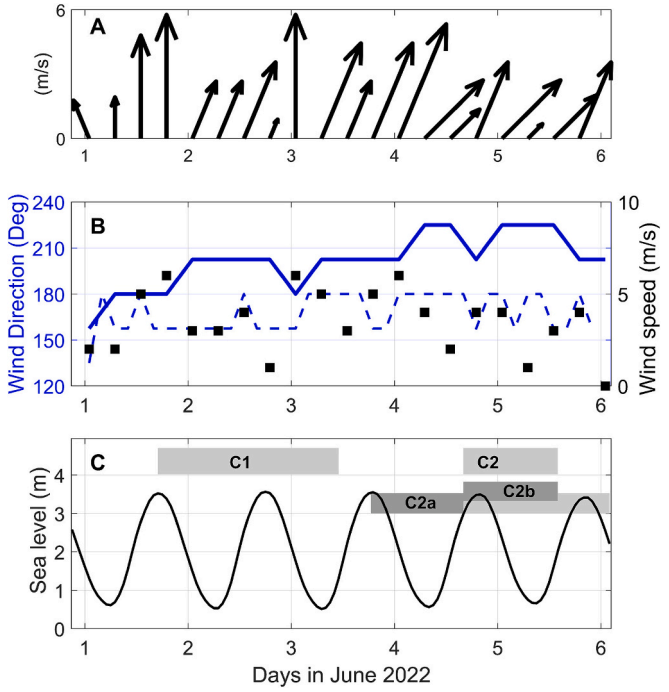

Fig. 2. (A) Wind during the study period, observed at the Hon Dau Island meteorological station.
(B) Wind speed (black squares) and direction (blue solid line) at Hon Dau station, and wind direction at Long Vy offshore meteorological station (blue dashed line). (C) Sea level variation at Hon Dau Island tidal station. Grey shading shows the time interval of velocity observations by drifting buoys in different clusters. (For interpretation of the references to color in this figure legend, the reader is referred to the web version of this article.)

peninsula (Fig. 1b). Tidal motions in the GoT are diurnal with the dominant constituents O1 and K1 having amplitudes much larger than those of M2 and S2 (by a factor of 4 and 10 respectively) Nguyen-Duy et al., 2021).

The wind conditions during the study period were typical for the Asian summer monsoon, with persistent southerly winds in this region (Fig. 2a). A diurnal variability in wind speed was also observed, with a slightly higher speed at the end of the day. The wind veered to the northeast from June 3 onwards (Fig. 2a). What is more interesting is that the wind veering was not detected at the offshore meteorological station Long Vy (Fig. 2b), located about halfway between Cat Ba and Hainan Island (China). This may indicate the existence of a local circulation influenced by the site's orography.

2.2. Surface velocity data and salinity profiles

A total of three clusters (referred to hereafter as C1, C2a, and C2b), with two to five buoys in each, were released in the RR plume region during a sea survey conducted on June 1–5, 2022. Cluster C1, composed of five buoys, was released at high water (HW) on June 1, 2022, 17:00 LcT (local time) and tracked for 42 h. Tracking duration ranged from 22 h for cluster C2b (3 buoys) to three weeks for cluster C2a (2 buoys), with overlapping periods (Fig. 2c). The release of clusters C2a and C2b was in the same location, at HW, but separated by approximately one tidal period (precisely by 22 h). Wind conditions were also similar during the drift of buoys in both clusters. Therefore, the trajectories of cluster C2a, from release to 22 h of drift (orange lines in Fig. 1b; dark grey shading in Fig. 2c), were combined with those of cluster C2b (green lines in Fig. 1b; dark grey shading in Fig. 2c). The five buoys were thus grouped as cluster C2 (Fig. 2c). Since their trajectories remained sufficiently close after release, all ten buoy pairs within C2 were analyzed together. The initial separation between all pairs of drifters was approximately 500 m.

Surface drifters of two types were used: the coastal Nomad surface buoys, cylinder-shaped, and manufactured by SouthTek (https://www.southteksl.com), equipped with GPS/GSM transceiver, and home-made drifters, equipped with GPS/satellite transceiver SmartOne using the satellite network GlobalStar. The design of home-made drifters was similar to that of coastal Nomad drifters, i.e., a cylindrical PVC hull of 0.6 m long and 0.1 m in diameter weighted in its lower part. A thin square plate of 0.3×0.3 m^2 in size was installed in the upper part of the hull to assure better stability in the vertical and to reduce the pitch. All drifters were equipped with a drogue of 0.5 m long positioned in the water column between 0.8 and 1.3 m depth, allowing them to drift with surface currents, and to minimize the motion due to windage. Drifter locations were available at time intervals varying from 5 to 15 min. The acquired geographic coordinates were re-sampled at a regular time step of 30 min; the resulting trajectories are shown in Fig. 1b.

A large number of CTD casts with the SonTek CastAway probe were done during the survey period. Salinity profiles obtained at rising tide along a transect in the near-field of the plume are shown in Fig. 3. The plume thickness did not vary much, from 4 m near the shore to 2.5 m 8 km offshore. On the contrary, the salinity in the surface layer increased from 0 to 15, showing high salinity gradients along the transect. The background salinity in the lower layer was around 30 (Fig. 3a). Other profiles available in a larger area indicated offshore expansion of the RR plume (not shown).

In addition, underway velocity measurements were performed by towed ADCP (Teledyne/RDI 1.2 MHz workhorse Sentinel). Velocity profiles were acquired along the transect from the Van Uc river mouth to Hon Dau Island at 1 s resolution in time and 0.5 m in the vertical, then averaged in the 1 m deep surface layer (from 0.5 to 1.5 m) and over 1 min. The resulting velocity vectors, shown in red in Fig. 3b, were used to reconstruct a surface current vector map by applying the 2dVar variational interpolation method (Yaremchuk and Sentchev, 2009). 2dVar is a non-local method of interpolation. It uses all velocity measurements in combination with the dynamic constraints (divergence, curl, and zero velocity component normal to rigid boundaries) to obtain a velocity vector at each grid point. The resulting field best fits the observations and captures small-scale velocity variations that are resolved by the variational approach but are difficult to reproduce using other interpolation methods. The current map in Fig. 3b represents the combined influence of tidal currents and river runoff and provides a comprehensive view of the spatial variation in coastal flow during the rising tide on 4 June 08:30–13:00 (low water at 07:00). Large current velocity values, up to 0.7 m/s, were observed at two locations, namely at the river mouth and in the coastal jet, roughly following the bathymetry contours from 5 to 10 m (Fig. 3). Large velocity variations across the jet are a characteristic feature of the observed coastal current. The relative error of interpolation, evaluated by projecting the interpolated velocity vectors onto the observation locations and calculating the difference, was low (19 %), indicating a high level of confidence in the reconstructed current field.

2.3. Circulation model SYMPHONIE

The 3D hydrodynamic model SYMPHONIE is a Boussinesq hydrostatic coastal circulation model based on an Arakawa curvilinear C-grid (Marsaleix et al., 2008). The model configuration used in this study is is identical to that described by Nguyen-Duy et al. (2021, 2023) and Tran et al. (2022). A detailed description of the model and its validation is provided in Nguyen-Duy et al. (2021). Here, we summarize only the key information of the model configuration. The SYMPHONIE model employs the k–ε turbulence closure scheme and the QUICKEST scheme for tracer advection and diffusion (Neumann et al., 2011). Specifically, QUICKEST uses a fourth-order centered scheme for horizontal advection

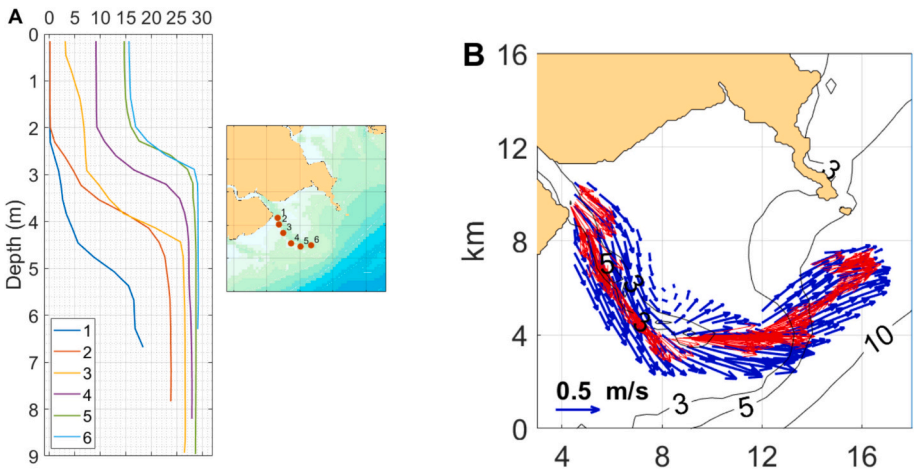

Fig. 3. **(A)** Salinity profiles (left panel) along the transect shown by red dots in the right panel (stations numbered 1 to 6), measured on June 4, 2022, 08:30–13:00 during the rising tide. Bathymetry is shown by color shading. **(B)** Surface current velocities recorded by towed ADCP (red arrows) along the same transect. Spatially interpolated velocities are shown by blue arrows. Grey lines indicate the 3, 5, and 10 m depth contours. (For interpretation of the references to color in this figure legend, the reader is referred to the web version of this article.)

of momentum, a bi-harmonic scheme for horizontal diffusion of momentum, and a second-order centered scheme for vertical advection of momentum. This hybrid formulation ensures good model stability across a wide range of Courant numbers. A more detailed description of QUICKEST and its implementation in the model can be found in Garinet et al. (2024, Section 2.3.2). The grid resolution increases gradually from 300 m locally near the shore in the Red River delta to 4500 m toward the deeper part of the gulf, at the open boundaries (Fig. 1a). In the vertical direction, 20 seafloor following levels define a variable vertical resolution. The enhanced resolution in the western part of the gulf (Fig. 1a) was sufficient to resolve motions at scales comparable with the first baroclinic Rossby radius of deformation (Nguyen-Duy et al., 2021). The model bathymetry has been progressively refined by integrating various datasets and increasing spatial resolution. This refinement is essential for the reliable simulation of currents and mixing.

Atmospheric forcing is introduced via the bulk formulae of Large and Yeager (2004) using the 3-hourly outputs of the ECMWF 1/8° atmospheric operational analyses. Initial conditions and lateral open boundary conditions are prescribed from the daily outputs from the operational Mercator global ocean analysis and forecast system at 1/12° provided by the Copernicus Marine and Environment Monitoring Service (CMEMS). Tidal data were taken from the global atlas FES2014 (Lyard et al., 2021). Nine tidal constituents have been considered. River forcing was enabled, with the information of river systems along the coasts of the GoT described in detail in Nguyen-Duy et al. (2021).

The model configuration used in our study has been extensively validated by Nguyen-Duy et al. (2021) and Piton et al. (2021) through comparisons with multiple observational datasets, including: (a) temperature–salinity profiles collected in the study region during the VITEL campaign in 2014; (b) surface velocity measurements from HF radars (a one-year time series of daily averaged velocities); and (c) amplitudes of the major tidal constituents that dominate sea surface height variability in the Gulf of Tonkin (GoT). Discrepancies were quantified, and the results demonstrated good model performance.

The SYMPHONIE model was run over 2021–2022. Surface velocity fields in a sub-domain of limited size (Fig. 1b) were extracted from the hourly instantaneous model outputs and interpolated onto a regular 0.5 km grid. These fields were then used for particle tracking, for comparing virtual and real drifter trajectories, and for subsequent analyses.

Virtual drifter trajectories in the model velocity fields were computed by the open-source software OpenDrift (https://opendrift.github.io/, Jones et al., 2016), using the 4th order Runge-Kutta scheme and bilinear interpolation. The horizontal diffusion parameter was set to 0. In OpenDrift, particles were initially put at the time and location of the real drifters to calculate the separation distance between the real and virtual trajectories. The maximum and mean velocity (time and drifter averaged) were estimated and used for assessing the model performance.

2.4. Lagrangian diagnostics

In a turbulent ocean flow, a cluster of neutrally buoyant particles carried by the current undergoes spreading, the intensity and direction of which depend on a number of factors, such as the distribution of energy across scales of motion, the presence of current convergences, indicating the location of frontal zones, external forcing, bathymetric constraints (for coastal regions), etc.

Absolute dispersion $A^2(t)$ is generally used to extract information about the largest and most energetic scales of motion acting to transport particles over long distances. It is defined as the variance of particle displacements from their initial positions at the initial time t_0, i.e. the release time. In a two-dimensional flow, occupying the surface layer, for example, absolute dispersion can be estimated in the zonal (along x-axis) and meridional (along y-axis) directions following the expression (e.g., Enrile et al., 2019):

$$A_{ij}^2(t) = \frac{1}{N}\sum_{k=1}^{N}\left\{\left[\boldsymbol{x}_i^k(t)-\boldsymbol{x}_i^k(t_0)\right]\left[\boldsymbol{x}_j^k(t)-\boldsymbol{x}_j^k(t_0)\right]\right\}A^2(t) = A_{xx}^2(t)+A_{yy}^2(t), \quad (1)$$

where $i,j = x,y$, N is the total number of particles in a cluster, $\boldsymbol{x}^k(t)$ is the position vector, of coordinates (x, y), of the k-th particle at time t, and $\boldsymbol{x}^k(t_0)$ is that at the release time.

At time scales smaller than the Lagrangian correlation time, absolute dispersion is expected to grow quadratically in time: $A(t)^2 \sim t^2$, indicating a ballistic regime of dispersion. The ballistic regime lasts as long as the trajectories save some memory of their initial conditions. In the opposite limit of large times, when the particle velocity autocorrelation is close to zero and the memory of the initial conditions is lost, absolute dispersion becomes a linear function of time, $A(t)^2 \simeq 2K\,t$, where the proportionality coefficient K is the absolute diffusion coefficient, introduced by Taylor (Taylor, 1922).

The use of two-particle Lagrangian diagnostics, such as relative dispersion $R_d^2(t)$ or the finite-size Lyapunov exponent, λ, allows to extract information about the physical mechanisms governing the separation of particle pairs, and to associate the latter with the different

flow scales. For this purpose, relative dispersion is commonly used. It is defined as the squared separation distance between particles k and l in a pair at time t, averaged over all particle pairs:

$$R_d^2(t) = \frac{1}{N(N-1)} \sum_{kl}^{N} \| \boldsymbol{x}^k(t) - \boldsymbol{x}^l(t) \|^2 \quad (2)$$

The behavior of relative dispersion depends on the level of turbulence in the flow field, usually quantified by the turbulence kinetic energy spectrum $E(k)$, where k is the (horizontal) wavenumber modulus. At short times, when the pair separation distance is small, the evolution of relative dispersion follows a ballistic behavior, $R_d^2(t) \sim t^2$. This regime also occurs in strong and persistent currents, or coastal jets, where the major source of the velocity variability and dispersion are large horizontal velocity gradients (LaCasce, 2008). Richardson superdiffusive regime corresponds to $R_d^2(t) \sim t^3$ and occurs at larger time scales, in sufficiently energetic flow, i.e. when $E(k) \sim k^{-5/3}$ (e.g., Foussard et al., 2017). In this case, the dispersion of particles is controlled by eddies with a size similar to the mean separation distance between pairs of particles. For less energetic spectra, steeper than k^{-3}, instead, relative dispersion grows exponentially in time. When the particle separation reaches scales much larger than the largest characteristic flow scale, the pair velocities become uncorrelated and a diffusive regime with scaling $R_d^2(t) \sim t$ is expected.

Relative dispersion can be also seen as the dispersion of particles in a cluster with respect to the mean particle position at time t (cluster barycenter) and quantified by the variance of particle positions. Depending on the geography of the coastal zone studied and the dominant direction of the flow, such variance is sometimes calculated in the direction of maximum particle spreading and in the perpendicular direction, providing two quantities, $R_1^2(t)$ and $R_2^2(t)$, which account for dispersion along these two axes. R_1 and R_2 are estimated by applying the Principal Component Analysis (PCA) to the spatial particle distribution at each time step (Thomson and Emery, 2014):

$$\begin{bmatrix} R_1^2 \\ R_2^2 \end{bmatrix} = \frac{1}{2} \left[\left(\overline{x'^2} + \overline{y'^2} \right)^2 \pm \left(\overline{x'^2} - \overline{y'^2} \right)^2 + 4 \left(\overline{x'y'} \right)^2 \right], \quad (3)$$

where $\overline{x'^2}$, $\overline{y'^2}$ and $\overline{x'y'}$ represent the variances of particle positions in the x and y directions, and their covariance, respectively.

The orientation of the resulting dispersion ellipse (i.e., the orientation of R_1 axis with respect to the x-axis direction) is given by:

$$\Theta(t) = \frac{1}{2} tan^{-1} \left[\frac{\overline{2x'y'}}{\overline{x'^2} - \overline{y'^2}} \right], \quad (4)$$

The Finite Size Lyapunov Exponent (FSLE), λ, is estimated by measuring the inverse of the time τ, during which the distance between two fluid particles grows from a value δ_k to a larger one $\delta_{k+1} = r\,\delta_k$ (with $r > 1$, $k = 1, \ldots, N_k$ and N_k the number of values, chosen in a way to span the relevant range of scales):

$$\lambda(\delta) = \frac{1}{\langle \tau(\delta) \rangle} ln\, r. \quad (5)$$

Here, brackets represent an average over all particle pairs. Values of λ can be also used to characterize the regime of dispersion (see, e.g., LaCasce, 2008; Berti et al., 2011; Schroeder et al., 2012). Compared to relative dispersion, the FSLE, being a fixed-length indicator, better allows to disentangle contributions of different scales of motions to dispersion (Artale et al., 1997). A sensitivity analysis of the results to the choice of r was performed with the fixed number of particles in the area. It was found that varying r from 1.2 to 1.6 does not change the slope of $\lambda(\delta)$ considerably and the value of $r = 1.4$ was finally adopted.

In addition, the spatial distribution of the backward FSLE estimate (different from the particle-pair-averaged FSLE described above) has been obtained in order to characterize the intensity of stirring and horizontal spreading over the RR plume region. This diagnostic is frequently used to quantify transport and horizontal mixing in the ocean (e.g., d'Ovidio et al., 2004; Hernández-Carrasco et al., 2011; LaCasce, 2008; Tran et al., 2022). In these and several other studies, the authors demonstrated that the largest backward FSLE values concentrate along characteristic lines, identifying regions of maximum stretching, which correspond to specific dynamic features, such as fronts, or current convergence zones, named attracting Lagrangian coherent structures, aLCS (Hernández-Carrasco et al., 2018). It was demonstrated that such aLCS can act as barriers to transport and strongly affect the spatial distribution of particulate material in the ocean surface layer.

FSLE maps were then estimated at position $\boldsymbol{x}$ as the inverse of the time $\tau(\boldsymbol{x})$ required for two particles of fluid to separate from an initial distance δ_0 to a final distance δ_f:

$$\lambda(\boldsymbol{x}) = \frac{1}{\tau(\boldsymbol{x})} ln \left(\frac{\delta_f}{\delta_0} \right). \quad (6)$$

In this study, the algorithm described in Hernández-Carrasco et al. (2011) was used, with δ_0 set to 0.5 km (the grid size), $\delta_f = \alpha\, \delta_0 = 2.5$ km, and the amplification factor $\alpha = 5$, enabling to measure important stretching rates and obtain reliable aLCS. Backward FSLEs were obtained by advecting particles backwards in time for a time period of 5 days, comparable to the survey duration.

3. Results

3.1. Lagrangian dispersion characterization from time dependent indicators

The trajectories of two clusters of surface drifters and the corresponding ones from model simulations were used to assess the flow dynamics and Lagrangian dispersion in the RR plume region. A total of five buoys of cluster C1 and five buoys of cluster C2 were released in front of the Van Uc river estuary. The buoys of C1 moved north-eastward during approximately 24 h after release, under the effect of tide and southern wind. At the end of the 24 h period, three buoys beached in a very shallow-water area in the vicinity of Cat Ba Island, while the two remaining drifters started moving southward after the current reversal of HW on June 2, 2022, 18:00 (Fig. 4a). The mean and maximum speeds of drift were found to be 0.24 and 0.6 m/s respectively (Table 1).

Absolute dispersion followed two regimes (Fig. 5a). During the first 10 h, we found that $A^2 \sim t^2$, with larger dispersion in the zonal direction. The best fit with a quadratic function yields a prefctor of 1.3 km^2/h^2, which has a physical meaning. It accounts for the Lagrangian velocity variance, i.e., twice the kinetic energy measured by the drifter trajectories. From 10 h onward, absolute dispersion evolves as a linear function of time ($A^2 \sim t$) indicating a diffusive behavior. Therefore, the Lagrangian correlation time appears short, of the order of 10 h.

Relative dispersion, which was first quantified along the major and minor axes of spreading (R_1^2, R_2^2), then combined to obtain $R^2 = R_1^2 + R_2^2$, also showed two regimes. During 6 h after release, the buoys did not separate much, and the shape of the cluster remained almost unchanged. When the buoys passed the alignment of Do Son peninsula and Hon Dau Island (Fig. 5c), R^2 followed a ballistic regime, scaling as t^2, and appeared highly anisotropic. Spreading was found ten times larger along the major axis of dispersion (R_1^2), roughly oriented across the line of buoy travel (Fig. 5c). Fairly high horizontal velocities and non-negligible cross-jet velocity gradients, measured by towed ADCP in the coastal area (Fig. 3b), are likely the main cause of enhanced spreading across the dominant flow direction, i.e., shear dispersion.

The capability of the numerical model to reproduce the properties of the underlying turbulent flow was assessed in two ways by performing particle-tracking experiments. First, five particles (virtual buoys) were placed in real drifter locations and tracked during 30 h. The mean separation distance between the real and virtual buoys was estimated (Table 1). The ensemble-averaged travel distance and final separation

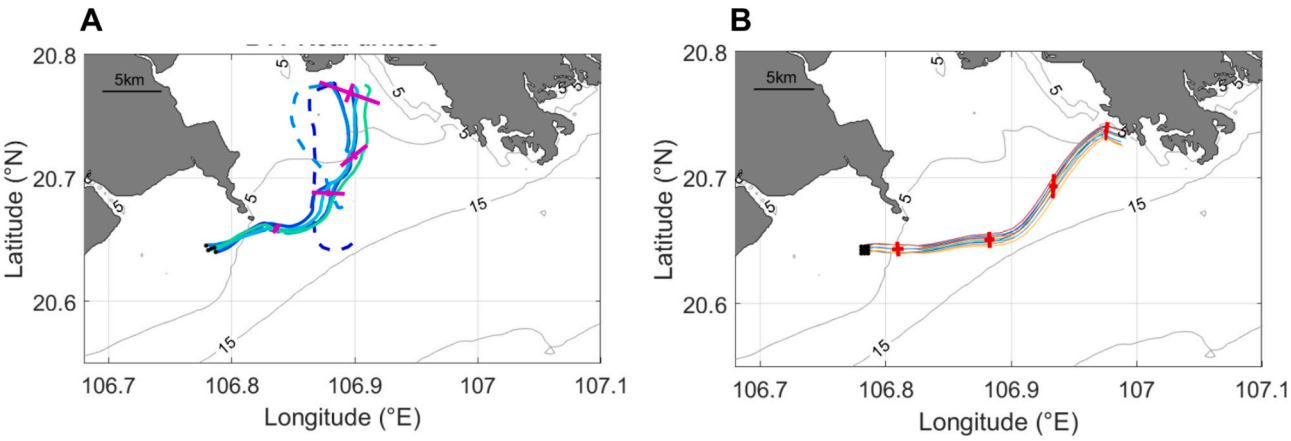

Fig. 4. Trajectories of five surface drifters in cluster C1, released at high tide on June 1, 2022, 17:00 (A), and model trajectories of nine drifters, initially spaced by 300 m and released at the same time and location as the real drifters in C1 (B). Major and minor axes of spreading are shown by magenta and red lines at 6 h intervals. The parts of two trajectories shown by dashed lines were excluded from the analysis. (For interpretation of the references to color in this figure legend, the reader is referred to the web version of this article.)

Table 1
Drift time, drift distance, mean and maximum drift speed of surface buoys in clusters C1 and C2 (ensemble averaged) from observations and model simulations (values in parentheses), and the mean separation distance between observed and simulated buoy trajectories.

Cluster	Nb of buoys	Drift time (h)	Drift distance (km)	Mean speed (m/s)	Max speed (m/s)	Mean separation distance (km)
C1	5	28–42	55 (58)	0.26 (0.25)	0.55 (0.52)	3.7
C2	5	22	54 (51)	0.42 (0.32)	0.62 (0.46)	5.7

from the real drifters were 58 km and 3.7 km, respectively, corresponding to a relative error of about 6–7 %. The virtual buoys followed the trajectories shown in Fig. 4b, which were longer and more northeast-oriented than those of the real drifters. The mean and maximum drift speed were equal to 0.25 and 0.52 m/s, respectively, which are quite similar to those derived from observations (Table 1).

In the second step, Lagrangian dispersion was assessed using nine particles released in a square area and initially separated by 0.3 km (a 3 × 3 cluster of regularly spaced particles). The cluster location and the time of release exactly matched those of the real drifters. A larger number of particles was used to improve the statistical robustness of the estimates.

The time evolution of the absolute dispersion of virtual buoys is likely to follow a quadratic law ($A^2 \sim t^2$), for most of the period of simulation (Fig. 5b). As the virtual buoys approached Cat Ba Island, a change in the velocity field due to topographic constraints led to a decrease in the rate of dispersion. Some buoys beached, while others continued to drift along the island. As a result, after hour 22, the slope of the A^2 curve shows a little change tending to t, indicating a longer Lagrangian correlation time than that obtained by analyzing real-drifter dispersion. The consequence of the longer correlation time is a significantly higher intensity (50 % higher) of absolute dispersion in the model simulations at the end of the 25 h period (Fig. 5b). The anisotropy of dispersion also appears more important in the model. The level of kinetic energy in the model simulations was found similar to that revealed by observations: 1.3 and 1.4 km^2/h^2, respectively (Fig. 5a,b)

The major and minor axes of the relative dispersion of virtual buoys from model simulations are shown in Fig. 4b. Detailed comparison with real drifters revealed that relative dispersion evolves in a similar way, with very low dispersion during the first 10 h (dispersion rate close to zero), before the onset of a ballistic regime during the next 10 h (Fig. 5d). The decrease in dispersion rate, observed around 20 h, is due to the arrival of buoys into very shallow waters near Cat Ba Island, where the current speed and dispersion rate dropped. Dispersion becomes anisotropic a few hours after the release. As in the case of real drifters, the principal axis of dispersion, oriented from south to north, is globally transverse to the drifter trajectories. The ratio between dispersion along the two principal axes reaches an order of magnitude, 15 h after release.

Lagrangian dispersion in the RR plume region was also assessed for the second period of the survey, when the wind veered to the northeast (Fig. 2a). To improve the robustness of statistical estimates, two buoys released on June 3 and three buoys released on June 4 were combined to form cluster C2, as described in section 2.2. The trajectories obtained (Fig. 6a) are interesting because they show a significant change in the direction of surface currents on these two dates, caused by the change in wind direction toward the northeast, as compared to that observed on June 1 (Fig. 2). The wind not only produced a seaward extension of the plume, but it also significantly increased the rate of spreading of the drifting buoys.

Absolute dispersion was found to be higher for C2 than for C1, reaching maximum values of 800 and 350 km^2, respectively (Fig. 7a and Fig. 5a). It was largely anisotropic, with the dominant zonal component (A^2_{xx}) aligned with the seaward flow direction. The ballistic regime, scaling as t^2, was observed from the very beginning until later stages of the dispersion process.

On the contrary, the range of variation of relative dispersion is rather similar to that found from C1, i.e. from 0.1 to 3 km^2 at the end of the 20 h time period (Fig. 5c and Fig. 7c). It is difficult to identify the regime of dispersion of buoys during 10–12 h after release. The drift of the buoys was affected by Hon Dau Island, which canalizes the flow within a 1 km-wide strait and also in a very shallow-water area south of the island. Ten hours after release, dispersion approaches to some extent the ballistic regime ($R^2 \sim t^2$), but the data do not allow to draw a completely clear conclusion. During this period, the dispersion is not exactly monotonic, probably due to differences in the drift velocity of buoys launched on two successive dates, June 3 and 4. The relative dispersion of C2 is characterized by a high degree of anisotropy (one order of magnitude), with the major axis of spreading oriented along the flow direction (Fig. 6a).

The model simulation of Lagrangian dispersion of nine virtual drifters shows a good overall agreement with observations in terms of drift speed and direction, distance (Table 1), spreading, and degree of anisotropy (Fig. 6). The regime of dispersion was close to ballistic (scaling larger than t^2) during most of the drift time, from 5 to 18 h

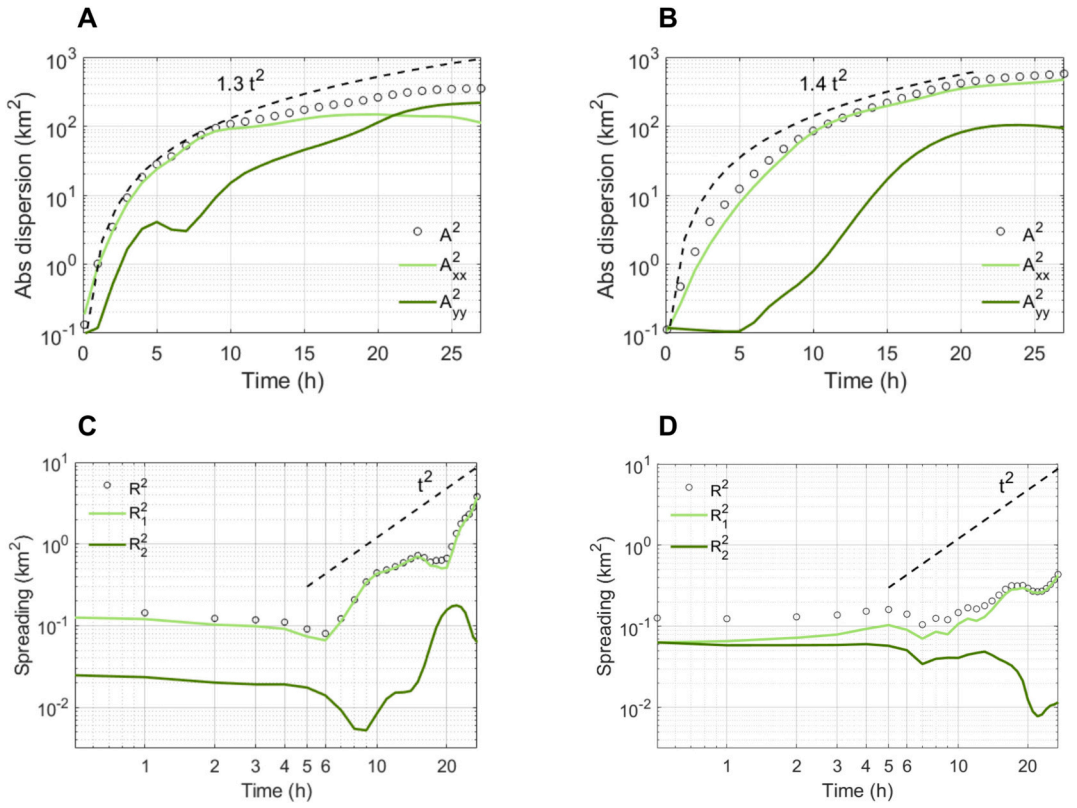

Fig. 5. Absolute dispersion A^2 of five real drifters in cluster C1 (A) and of nine virtual drifters released at the same location (B). Relative dispersion (total and along the major and minor axes of spreading) for real (C) and virtual (D) drifters. Black dashed lines show the best fit of A^2 and R^2 by a quadratic function.

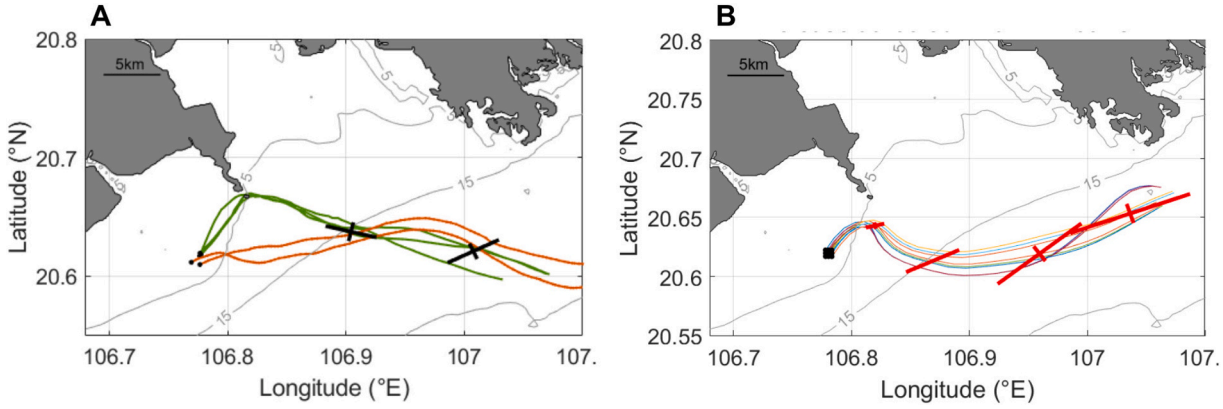

Fig. 6. Trajectories of surface drifters released at high tide on June 3, 2022, and on June 4, 2022 (orange and green lines, respectively) (A), and model trajectories of nine drifters, spaced by 300 m and released at the same location as the real drifters on June 3, 2022 (B). Major and minor axes of spreading are shown by black and red lines at 6-h intervals in (A) and (B), respectively; axes of spreading of real drifters 6 h after release in (A) are not shown. (For interpretation of the references to color in this figure legend, the reader is referred to the web version of this article.)

(Fig. 7d). However, starting from time 10 h, the intensity of relative dispersion was found twice higher in model simulation. On the other hand, absolute dispersion (Fig. 7b) shows a very similar trend to that obtained from observations. Overall, the results of the comparison demonstrate the model capability to reconstruct not only reasonably well a complex coastal flow pattern but also absolute dispersion, as well as some qualitative aspects of relative dispersion.

3.2. Scale dependent dispersion

To further assess dispersion regimes and to identify the characteristic scales of the underlying turbulent flow, the FSLE, λ(δ), was computed using the trajectories of real drifters and the corresponding trajectories of nine virtual drifters advected in the model velocity field (Fig. 6).

The analysis of C1 trajectories revealed that, during five hours after release, as the buoys move eastward at high speed ~0.4–0.5 m/s (from HW at 17:00 to 22:00), the mean separation distance between particle pairs does not increase but, on the contrary, decreases (Fig. 4c). This suggests that the flow field is strongly affected by topographic features, in particular, by Hon Dau Island (Fig. 4a). Therefore, the FSLE (Eq. 5) was estimated starting from 22:00, when drifters actually started to separate.

The scaling behavior of λ(δ) reveals a ballistic regime of dispersion ($\lambda(\delta) \sim \delta^{-1}$) at all scales, from 0.35 km to ~3 km (Fig. 8). Its

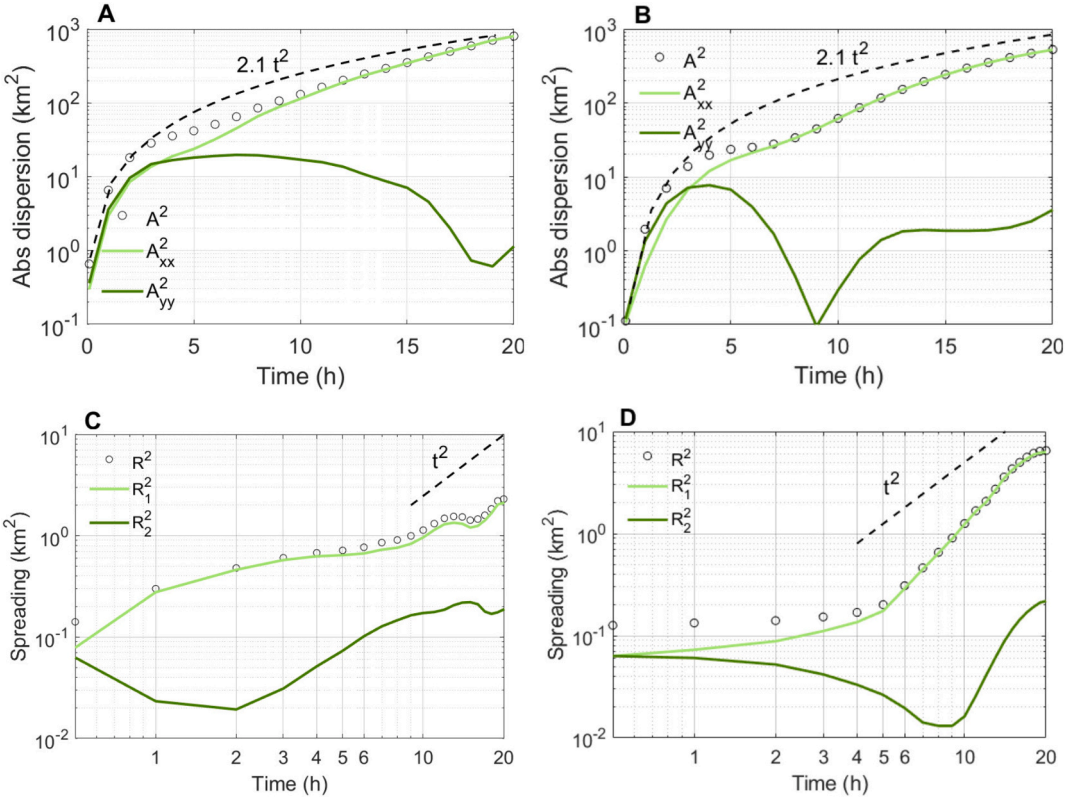

Fig. 7. Absolute dispersion A^2 of five real drifters in cluster C2 (A) and of nine virtual drifters released at the same location (B). Relative dispersion (total and along the major and minor axes of spreading) for real (C) and virtual (D) drifters. Black dashed lines show the best fit of A^2 and R^2 by a quadratic function.

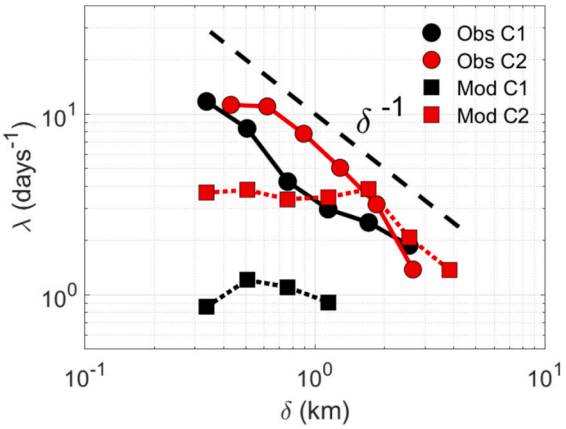

Fig. 8. Finite-size Lyapunov exponent λ(δ) as a function of the separation distance δ, for drifters in clusters C1 and C2 (circles), and virtual drifters advected in the model velocity field (squares). The δ^{-1} behavior (black dashed line) indicates the ballistic dispersion regime.

predominance implies that the pair-separation process is controlled by a scale independent velocity increment presumably associated with the current jet. This result is also supported by the spreading in time of buoys in C1, which was well approximated by $R^2 \sim t^2$ (Fig. 5c). No change of dispersion regime was observed because of the relatively short duration of advection. The FSLE obtained from drifter pairs in C2 revealed globally similar results (Fig. 8). Also in this case, the behavior of λ(δ) indicates a ballistic regime of dispersion at all scales. The typical dispersion rate from observations appears quite high, with the largest values reaching $\lambda_{max} \approx 10$–13 day^{-1}.

Unlike real observations, the model simulations of nine drifter trajectories at the beginning of the survey (June 1–2), do not allow to quantify satisfactorily the scale dependent dispersion rate. The FSLE curve appears quite flat and scale independent (Fig. 8, black squares). Moreover, the intensity of virtual drifter separation processes, represented by λ(δ), was found in the model simulations significantly lower ($\lambda_{max} \approx 3$ day^{-1}) than that revealed by observations ($\lambda_{max} \approx 13$ day^{-1}). This may be probably related to difficulties of the model in capturing properly the very fine-scale spatial structure of the velocity field in the plume body, under a persistent southerly wind.

On the contrary, modeling of virtual drifter trajectories on June 3–4, when the wind veered northeast, provided much better agreement with observations (Fig. 8). In particular, for large separations, the ballistic regime of dispersion is found and the λ(δ) curves from observations and modeling are in close agreement. On scales smaller than 2 km, the FSLE from model trajectories of C2 is still smaller than that from real-drifter data, though higher than that of C1, and levels off, again pointing to an underestimation of model velocity increments at small scales. Overall, these results demonstrate the capability of SYMPHONIE model to reconstruct coastal-flow dispersion properties reasonably well at relatively large scales in the submesoscale range.

3.3. *Spatial structure of Lagrangian dispersion from model simulations*

To assess the spatial variations of the dispersion process and to evaluate the combined effects of the RR outflow, tidal motions, and bathymetry constraints, two series of particle-tracking experiments were conducted. In the first one, passive particles were initially homogeneously spaced within the whole model domain and tracked in the model velocity field during a period of time corresponding to the surveying period. The aim of the experiment was to identify, throughout the study area, the location of zones of strong horizontal stirring (where particle spreading can be largely affected by spatial variations of the velocity field), as those suggested by the analysis of real and virtual trajectories presented above. Moreover, high stirring and spreading of

particles may indicate the presence of surface current convergence zones, which are ubiquitous in river plume regions. It is important to note that the model simulations accounted for variations in wind and tide, as well as daily fluctuations in RR discharge, which in turn modulated the seaward flow from the RR system.

The spatial distribution of FSLEs $\lambda(\boldsymbol{x})$ was obtained using the algorithm of particle tracking described in (Hernández-Carrasco et al., 2011) with the initial separation between particle pairs $\delta_0 = 0.5$ km and amplification factor $\alpha = 5$, enabling to achieve a reasonable stretching during the tracking experiments ($\delta_f = \alpha\,\delta_0 = 2.5$ km). FSLE maps were obtained by integrating particle trajectories backward in time over 3 days. Fig. 9a shows the FSLE spatial distribution at the end of the integration period. Lines with high $\lambda(\mathbf{x})$ values, known as ridge lines, delimit regions of high dispersion and stirring of particles along the attractive manifolds of the model velocity fields. In the RR plume region, several of such regions, each associated with distinct ridge lines, have been identified at different distances from the coast (Fig. 9a).

The mid-field of the Van Uc River plume is well delineated by semi-circular ridge lines, around 10 km from the coast, with the river mouth at their center. The shape of the area delimited by these lines, the total coverage and the distance from the shoreline, are all likely to correspond to the Van Uc river plume. Further offshore, at a distance from 15 to 25 km, there is another set of ridge lines, also of curvilinear shape. The latter probably marks the seaward limit of the Cam river plume, while the former is composed of two river plumes (the Van Uc and the Cam) merged together. It is worth noting that the second most important freshwater supply to the GoT comes from the Cam River (see Fig. 1b for river locations).

The ridge lines, shown in Fig. 9a, control particle spreading and typically act as barriers to the transport of floating materials. To demonstrate the role of FSLE ridge lines in structuring the spatial distribution of materials, a second particle tracking experiment was conducted. A cluster of 900 particles, initially spaced 150 m apart within a square area (shown in red in Fig. 9b) was released at the same time and place as those of C1 and C2 real drifters (on June 3, 2022, 18:30). The major and minor axes of particle dispersion are shown in red in Fig. 9c with a time step of 6 h. Twelve hours after release, dispersion starts to become strongly anisotropic, with the main axis of spreading roughly oriented across the flow direction. It is interesting to note that the dominant direction of spreading in the model simulation (Fig. 9c, red crosses) and that of the real drifters (Fig. 4a) are very similar. The spatial distribution of particles at two particular times, 15 h and 30 h after release, is shown by red dots in Fig. 9b. Obviously, the stretching of the particle cloud 15 h after release is strongly affected by the ridge lines located at a distance of 25 km from the Van Uc estuary. After 30 h this set of particles forms a curvilinear shape and its stretching appears to occur along a ridge line near Cat Ba Island. A large ridge line with the highest values of λ (up to 8 day^{-1}), oriented in south-north direction at a distance of ~25 km from the Van Uc river mouth, may considerably affect the spreading of particles if they are released from the Cam River estuary. Note that only values of $\lambda(\mathbf{x}) > 3.5$ day^{-1} are shown in Fig. 9b-d to indicate the location of zones where the current convergence is most likely to occur.

To explore Lagrangian dispersion in the southern part of the study area, a second cluster (cluster B), also containing 900 particles initially spaced by 150 m, was positioned within a square in front of Tra Ly river mouth, at a distance of 10 km from the coast (Fig. 9b). This southern part of the region does not contain ridge line of high λ values, except one located further offshore, probably delimiting the Ba Lat river plume expansion. The particles were released at the beginning of the rising tide, on June 2, 2022, 7:00 (LW + 1), and tracked during 38 h. The particle distribution 24 h and 38 h after release (Fig. 9b, magenta dots),

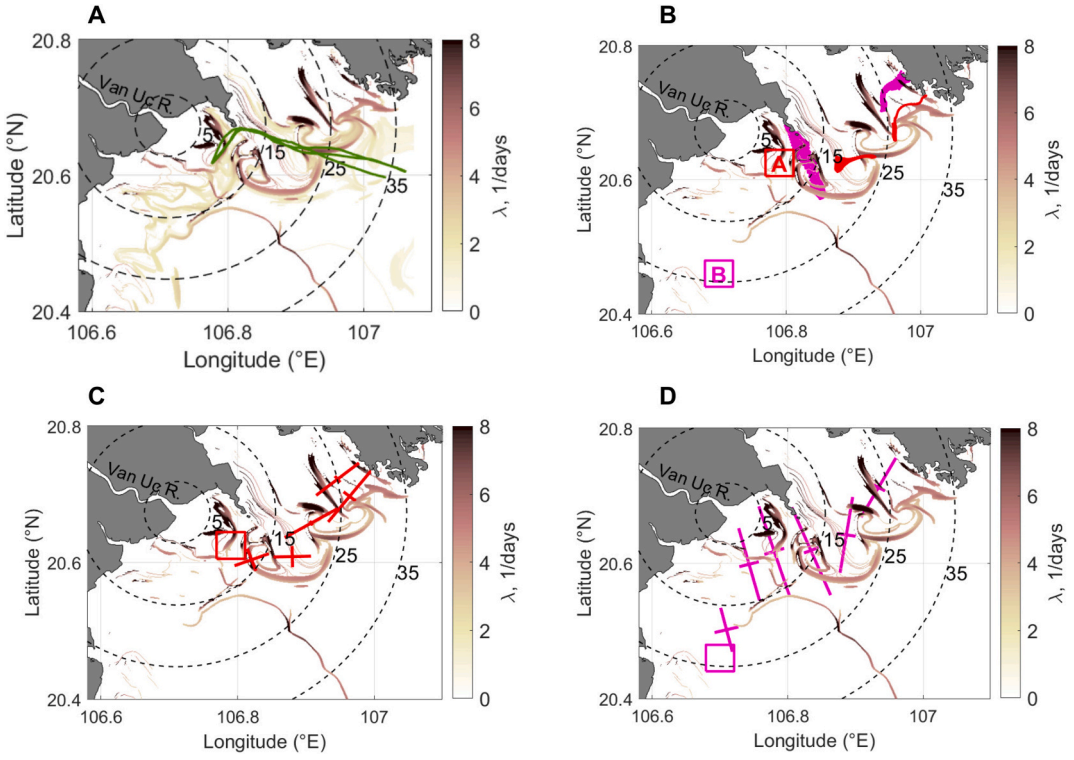

Fig. 9. (A) Spatial distribution of backward FSLE, $\lambda(\mathbf{x})$, in the RR plume region on June 3, 2022 from model simulations (color shading). Trajectories of surface buoys of C2b are shown in green. (B) Dispersion of 900 particles initially spaced by 150 m and released in areas A and B, shown by red and magenta squares respectively. The particle distribution 15 h and 30 h after release is shown in red for cluster A, and 24 h and 38 h after release in magenta for cluster *B. major* and minor axes of particle spreading ellipses are shown at 6 h intervals in red for cluster A (C) and in magenta for cluster B (D). Backward FSLE high values ($\lambda > 3.5$ day^{-1}) are shown by color shading in (B, C, and D). In all panels, dashed circles indicate the distance (in km) from the Van Uc river mouth. (For interpretation of the references to color in this figure legend, the reader is referred to the web version of this article.)

shows anisotropic dispersion, with spreading predominantly across the flow direction. The shapes formed by spreading particles apparently controlled by FSLE ridge lines during the drift. For instance, 24 h after release, the patch of particles was stretched, first along a curvilinear line, located at a distance of 10 to 25 km from the coast, then along a series of lines at the eastern side of the patch. After 38 h from release, particles are pushed against Cat Ba Island, resulting in a reduction of the patch size and of the length of the major axis of spreading (Fig. 9b,d). Fig. 9d shows the space-time evolution of particle spreading ellipses in more detail, revealing high anisotropy of dispersion, with a much stronger spreading in the direction of ridge lines located in the area between the Van River mouth and Do Son peninsula.

Particle trajectories of cluster B were used to characterize the regime of Lagrangian dispersion since the drift period was much longer than that in cluster A and the travel distance was also larger. The evolution of absolute dispersion is not monotonic (Fig. 10a). During first 11 h after release, a ballistic regime is found for particles in cluster B, with a quadratic increase of the distance from the release point. From 15 to 25 h, the evolution of absolute dispersion seems to become linear. On the whole, the ballistic regime seems to dominate. Fig. 10a also reveals that only the meridional component of dispersion (A^2_{yy}) slows down due to the presence of the coastline to the north, while the zonal component (A^2_{xx}) increases monotonically. Fitting absolute-dispersion data with a t^2 function in the southern part of the study area indicates that the level of kinetic energy of the coastal flow (prefactor 2.2 km^2/h^2) is similar to that revealed by drifter observations in the northern part under south-westerly winds (2.1 km^2/h^2), and significantly higher than that under southerly winds (1.4 km^2/h^2). This proves that wind has a decisive effect on dispersion and, more generally, on the behavior of the RR plume.

The time evolution of relative dispersion is shown in Fig. 10b. It provides indication that, from 6 to 15 h of the tracking period (particles drifting in the sector of the Van Uc river plume), the regime of relative dispersion is intermediate between ballistic and diffusive, scaling as $R^2 \sim t^{1.6}$. A change in regime is observed when the cluster of particles approached the Do Son peninsula, after about20 h. The flattening of the R^2 curve is probably due to the effects of the coastline and of the shallow depth, which reduce the velocity and the intensity of spreading in that area. Relative dispersion does not evolve much in the flow field of the Cam river plume, globally characterized by larger values of FSLE ridge lines, as shown in Fig. 9d. Here, the dispersion process could be strongly affected by topographic features and the presence of Cat Ba Island. However, it is difficult to characterize its regime in such a complex environment.

4. Discussion

In this study, a new method is proposed for characterizing the morphology of the Red River plume, during a summer season when freshwater discharge is large and conditions favorable to seaward plume expansion are met. The method employs the Lagrangian framework, and more specifically, Lagrangian particle tracking to estimate the separation distance and separation time between pairs of particles, in order to assess the properties of Lagrangian dispersion. An approach combining high-resolution numerical modeling and surface drifter observations has been adopted. The SYMPHONIE simulations have been validated using high-resolution velocity data from surface drifters deployed during an oceanographic campaign conducted in June 2022 in the plume region. The agreement was found to be good. For example, the largest relative error of separation was 10 %, mean and maximum drift velocities were comparable, and drifter trajectories were well reproduced in the model velocity field. Then the model was used to quantify Lagrangian dispersion, its time and scale dependence, as well as its spatial variability. All these estimates allowed us to quantify the intensity of stirring and horizontal spreading of passive particles across the extensive RR plume region, and to identify the plume expansion bounded by zones of surface current convergence, as indicated by FSLE ridge lines.

The Lagrangian diagnostics we have used, in particular the FSLE maps, $\lambda(\boldsymbol{x})$, are frequently employed to quantify horizontal mixing in the ocean and the effect of large stirring in the vicinity of current convergence zones on the spatial distribution of materials (e.g., d'Ovidio et al., 2004, 2015; Hernández-Carrasco et al., 2018, 2020; Tran et al., 2022). Lines of high λ values (ridge lines) are frequently associated with Lagrangian Coherent Structures (LCS) reflecting the spatial organization of the flow (e.g., Berta et al., 2014; Gough et al., 2016).

On large scales, the spatial distribution of FSLE ridge lines, obtained in the Mediterranean Sea by d'Ovidio et al. (2004), enabled to identify regions with very different mixing that exert a control on biological activity. That work opened the way for a more detailed assessment of the spatial distribution of biogenic materials, taking into account the dynamics and mixing properties in the basin. A similar methodology, applied on a regional scale in the southern Indian Ocean, has made it possible to monitor the dynamic boundaries between regions characterized by different mixing (d'Ovidio et al., 2015). In the western Mediterranean (Hernández-Carrasco et al., 2018) it allowed a better interpretation of physical mechanisms affecting phytoplankton dynamics and the patchiness of its spatial distribution. In those studies, fine-scale frontal zones, where surface currents converge, have been shown to act as barriers to the transport of biological material. On the contrary, Lagrangian coherent structures characterized by current divergence corresponded to zones with high Chl-a concentrations due to upward vertical velocities and the injection of nutrients into the surface layer (Hernández-Carrasco et al., 2018).

On smaller scales, surface current convergence (SCC) and the associated downward vertical velocities at the Mississippi river plume

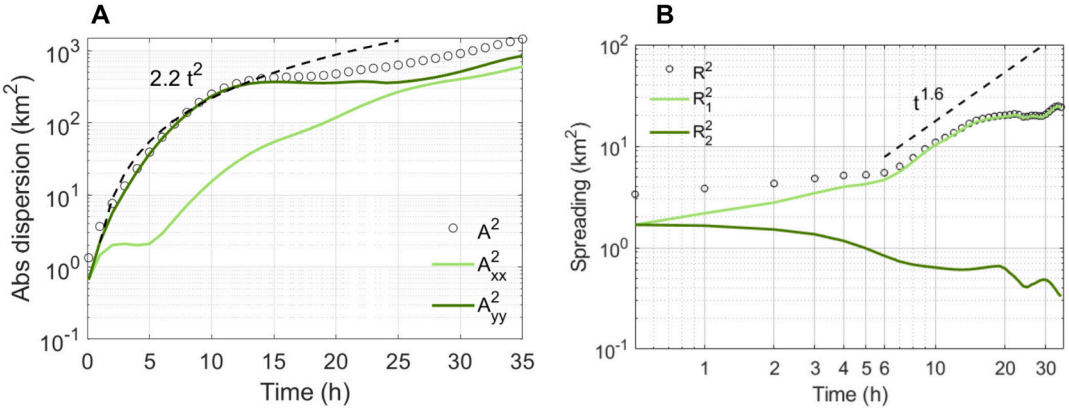

Fig. 10. Evolution of absolute dispersion (A) and relative dispersion (B) of 900 particles in cluster B, initially spaced by 150 m. The release location of particles is shown in Fig. 9b. Dashed lines show the best fit of A^2 and R^2 by power law functions.

boundary were documented in the observational study of d'Asaro et al. (2018). Their results provided, perhaps for the first time, observational evidence highlighting the importance of fine-scale attracting Lagrangian coherent structures, such as SCC, in concentrating materials floating with currents, even after significant spreading.

At regional scale in the Gulf of Tonkin, the modeling study of Tran et al. (2022) clearly demonstrated the effect of freshwater runoff on the spatial distribution of FSLE and the location of SCC in the gulf. The authors used high-resolution SYMPHONIE model simulations also to assess the seasonal variability of horizontal mixing and spatial distribution of SCC in response to the joint effect of the Asian monsoon winds and river runoff. In the studies mentioned above, the use of FSLE ridge lines has proved highly effective in identifying the location of SCC zones that can be viewed as boundaries separating areas with different dynamic regimes, as was highlighted by D'Asaro et al. (2018). The plume body and the seawater surrounding it are two water bodies with fundamentally different dynamics.

Our results revealed that a series of semicircular FSLE ridgelines located between 10 and 25 km offshore (Fig. 9a) represent the seaward boundary of the individual river plumes which, when merged, form the main body of the vast Red River plume. Dispersion of tracers (clusters of particles) in the model velocity field (Fig. 9b) and trajectories of real buoys (Fig. 9a) clearly show how FSLE ridge lines affect the transport of materials in the plume region: the buoy trajectories are indeed shaped by the FSLE ridge lines and closely follow them. Therefore, FSLE maps appear effective for assessing the structure of fluid transport and to reconstruct the morphology of the plume body.

SCC zones and enhanced stretching of passive tracer patches, obtained in model simulations, are the distinctive features of plume boundaries. Therefore, our results appear promising for the characterization of the morphology of river plumes in other geographic regions. To the best of our knowledge, the pioneering work of Tran et al. (2022) followed by our study, represent the first use of Lagrangian diagnostics, such as relative dispersion and FSLE, to characterize the role of horizontal mixing in structuring river plumes and dispersion of materials in coastal regions of Southeast Asia.

At the same time, other Lagrangian diagnostics, such as relative dispersion, R^2, absolute dispersion, A^2, and the space-independent, pair-averaged FSLE, $\lambda(\delta)$, have been used to quantify dispersion regimes and their scale dependence across the RR plume region. On short time scales, the ballistic regime was obtained in the lower submesoscale range (0.3–4 km) for both real and virtual drifters. This is expected in the presence of intense mean currents (LaCasce, 2008; Berti et al., 2011). A powerful coastal jet reinforced by the buoyancy input from the RR system and large gradients of the current velocity are probably the main causes. The intensity of relative dispersion, estimated from $\lambda(\delta)$, appeared high, with a maximum value $\lambda_{max} \approx$ 10–13 day^{-1}, from observations, but smaller ($\approx$ 3 day^{-1}) in simulations. Comparable values of dispersion rates were previously reported by Schroeder et al. (2012) in an observational study in the coastal region of the eastern Ligurian Sea (northwestern Mediterranean), where freshwater runoff from the Arno river (and several smaller rivers) formed a plume. With the exception of the runoff, which is much larger for the Red River, coastal hydrodynamics at the two sites can be considered similar. The important relative dispersion at submesoscales found in (Schroeder et al., 2012) was interpreted as Richardson dispersion, corresponding to $\lambda \sim \delta^{-2/3}$. Interestingly, realistic model simulations (ROMS was used) were unable to capture this enhanced dispersion regime, indicating the need for model refinement or better parameterization of sub-grid mixing.

Moreover, plume fronts are usually highly unstable and much narrower than the resolution of model grids. Therefore, high-resolution plume models must incorporate a more realistic representation of turbulence, accounting for physical processes that are not always resolved by the models but instead represented as subgrid mixing. One such process is the generation of internal waves by tidally pulsed plumes. These waves, whose presence has been documented through in-situ measurements in the Columbia River plume (e.g., Vlasenko et al., 2013) and the Winyah Bay plume (Yankovsky et al., 2022), enhance mixing at the outer edges of the plume and along intermediate fronts. A realistic representation of turbulence induced by frontal mixing and breaking internal waves requires a fully non-hydrostatic numerical approach. The non-hydrostatic version of the high-resolution MIT model, used by Stashchuk and Vlasenko (2009), and later by Vlasenko et al. (2013) to investigate the dynamics of the Columbia River plume, proved to be effective. Model simulations revealed the fine internal structure of the plume, including secondary fronts and internal wave systems propagating radially from the lift-off region to the outer plume boundary - features that were supported by observations. However, such modeling efforts remain computationally demanding and technically challenging, and there is little evidence that they would bring significant improvements in very shallow water regions, such as those considered in our study. At the same time, Garinet et al. (2024) demonstrated that the QUICKEST scheme implemented in the SYMPHONIE model produces excessive vertical mixing over highly variable seabed topography, where internal tides can develop. They further indicated that adopting a higher-order numerical diffusion operator can greatly improve the model's overall performance.

It is necessary to mention that our results demonstrated the capability of SYMPHONIE model to accurately reconstruct the dispersion regime in the coastal flow only in the upper submesoscale range (>2 km). At smaller spatial scales, model simulations showed that dispersion was scale independent, highlighting the strong influence of the model's limited resolution (~300 m near the coast) on its representation of lateral mixing. This conclusion is consistent with the findings of Choi et al. (2017), who investigated the effects of model resolution and river runoff on the spatial distribution of FSLE in the Gulf of Mexico.

In addition, our results revealed that relative dispersion is highly anisotropic, with values along the major axis being an order of magnitude larger than along the minor axis, the former roughly oriented across the main current direction. This is an example of shear dispersion, primarily driven by velocity differences across the coastal jet within the Red River (RR) plume. High anisotropy of horizontal relative dispersion was also obtained by Ohlmann et al. (2019) from observations in the western Gulf of Mexico. In that case, the predominant contribution to dispersion was observed in the direction perpendicular to the coastal flow direction. This may have important implications for pollutant-transport issues, such as the dramatic event "Deepwater Horizon oil spill" (e.g., Huntley et al., 2011), or the illegal discharge of toxic industrial waste into the ocean by the Formosa Group plant in Vietnam in 2016 (e.g., Do et al., 2023).

While our results confirm the model's overall skill, it is important to acknowledge that numerical simulations are subject to errors. For instance, Fig. 4 shows noticeable discrepancies between real and virtual drifter trajectories and dispersion ranges. Several factors may contribute to these differences, including uncertainties in forcing data, limitations in their spatial and temporal resolution, and simplifications in physical parameterizations, discussed above. The wind forcing is assumed to be the primary source of discrepancy. Using ensemble simulations with wind perturbations, Nguyen-Duy et al. (2023) performed a sensitivity analysis of regional circulation in the GoT to uncertainties in wind forcing. Their results showed that while the main characteristics of the RR plume are largely insensitive to wind perturbations, certain quantities, such as along-coast transport, are affected. Across the study region, the ensemble-based uncertainty in surface currents was estimated to range from 0.03 to 0.08 m/s. Furthermore, the dispersion rate of virtual buoys is strongly affected by Cat Ba Island (Fig. 4), which is represented in the model as a smoothed rigid boundary.

Several effective methods exist for reducing such discrepancies. For example, the study by Nguyen-Duy et al. (2023) on the impact of wind forcing uncertainties in the GoT provides a basis for future optimization of wind forcing. In another study, Tran et al. (2021) showed the benefit of surface current velocity measurements by HF radars along the

*V*ietnamese coast for reducing errors in SYMPHONIE model simulations arising from imperfect wind forcing.

5. Summary

By performing high-resolution simulations with the SYMPHONIE model, we have characterized the lateral mixing and morphology of the Red River (RR) plume in the northwestern Gulf of Tonkin from a Lagrangian perspective. During the study period, in June 2022, strong Asian monsoon winds drove seaward expansion of the river plume, accompanied by high freshwater inflow. Observations collected in the plume region during this period included high-quality surface velocity data from drifters and towed ADCP transects, complemented by CTD casts. The surface velocity field simulated by the SYMPHONIE model was validated against drifter observations, demonstrating its capability to reproduce coastal circulation and absolute dispersion with reasonable accuracy, as well as some qualitative features of relative dispersion.

FSLE ridge lines obtained from Lagrangian particle tracking revealed useful to demarcate the boundary between the plume body, originated from the individual river plumes of the RR deltaic system, and the surrounding seawater. The spatial distribution of FSLE enabled to identify the offshore expansion of individual plumes and revealed a variety of forms, semi-circular or hook-like filaments, characterizing the plume shape. A very good agreement between the spatial evolution of the FSLE and the motion of drifting buoys was obtained. In particular, the drifters followed FSLE ridge lines, confirming that these lines act as barriers to transport of mass, as well as of particulate and dissolved materials, and appear to be dynamic boundaries of the RR plume.

Within the plume body, the ballistic regime of dispersion dominated in the range of separations from 0.3 and 3 km (submesoscale range). No transition to other regimes, such as the Richardson regime, was observed over the analysis period, which was limited to 20–35 h. However, the analysis of relative dispersion using scale-dependent metrics, revealed high dispersion rates, with a maximum value $\lambda_{max} \approx$ 10–13 day^{-1}, retrieved from observations, and a much smaller one, $\approx$ 3 day^{-1}, from model simulations. Although such high dispersion rates are rarely observed, even larger values were reported in another coastal jet by Schroeder et al. (2012). The strong coastal jet is a characteristic feature of the RR plume in summer, and the associated velocity gradients were identified as the primary driver of shear dispersion across the flow. The pronounced anisotropy of dispersion has important implications for practical applications, including predicting the transport and fate of materials delivered to the sea by the Red River.

Lagrangian diagnostics, and in particular the FSLE, proved to be effective tools for identifying LCS and, consequently, for characterizing the morphology and spatial expansion of the RR plume. The spatial distribution of LCS provided insight into the surface circulation in ways that are not available with other types of analyses that can be applied to velocity fields provided by numerical models or HF radar observations, such as time-averaged vorticity, divergence maps, and mean flow. Extending LCS analyses and combining model simulations with other types of data, such as ocean color imagery, altimetry data, and HF radar velocity measurements will provide a more complete view of the coastal circulation and plume dynamics in this region, while also enabling potential model optimization. This will be the focus of future studies.

CRediT authorship contribution statement

Alexei Sentchev: Writing – review & editing, Writing – original draft, Visualization, Validation, Supervision, Software, Resources, Project administration, Methodology, Investigation, Funding acquisition, Formal analysis, Data curation, Conceptualization. **Thinh Nguyen-Duc:** Visualization, Formal analysis, Data curation. **Stefano Berti:** Writing – review & editing, Methodology. **Nadia K. Ayoub:** Writing – review & editing, Software. **Vu Duy Vinh:** Writing – review & editing.

Declaration of competing interest

The authors declare that they have no known competing financial interests or personal relationships that could have appeared to influence the work reported in this paper.

Acknowledgments

This research was funded by Vingroup Innovation Foundation (VINIF) under project code VINIF.2023.DA151. This work is also a contribution to the research activities of LMI LOTUS (http://lotus.usth.edu.vn). We would like to acknowledge the support from IRD (Institute of Research for Development) and CNRS, and from CNES (French Spatial Agency) via the SWOT COCTO-FO project. We warmly thank Sylvain Ouillon (IRD) for his strong involvement in organizing the sea campaign in *V*ietnam, Ismael Hernández-Carrasco for fruitful collaboration and providing us with his excellent Matlab code, and Eric Lecuyer (LOG) for assembling the buoys. We gratefully thank Patrick Marsaleix (LEGOS) and Nguyen Duy Tung (USTH) for their help with the SYMPHONIE model; the SYMPHONIE code is distributed by the SIROCCO French national service (https://sirocco.obs-mip.fr/), hosted by the Observatoire Midi-Pyrénées, Toulouse, France. The modeling work was granted access to the HPC resources of CALMIP supercomputing center under the allocation 2023-24-p1119. This study has been conducted using E.U. Copernicus Marine Service Information: (10.48670/moi-00016). The European Centre for Medium-Range Weather Forecasts (ECMWF, http://www.ecmwf.int) data is published under a Creative Commons Attribution 4.0 International (CC BY 4.0, https://creativecommons.org/licenses/by/4.0).

Data availability

Data will be made available on request.

References

Artale, V., Boffetta, G., Celani, A., Cencini, M., Vulpiani, A., 1997. Dispersion of passive tracers in closed basins: beyond the diffusion coefficient. Phys. Fluids 9 (11), 3162–3171. https://doi.org/10.1063/1.869433.

Ayouche, A., Charria, G., Carton, X., Ayoub, N., Theetten, S., 2021. Non-linear processes in the Gironde river plume (north-East Atlantic): instabilities and mixing. Front. Mar. Sci. 8, 701773. https://doi.org/10.3389/fmars.2021.701773.

Berta, M., Ursella, L., Nencioli, F., Doglioli, A.M., Petrenko, A.A., Cosoli, S., 2014. Surface transport in the northeastern Adriatic Sea from FSLE analysis of HF radar measurements. Cont. Shelf Res. 77, 14–23. https://doi.org/10.1016/j.csr.2014.01.016.

Berti, S., Alves Dos Santos, F., Lacorata, G., Vulpiani, A., 2011. Lagrangian drifter dispersion in the southwestern Atlantic Ocean. J. Phys. Oceanogr. 41, 1659–1672. https://doi.org/10.1175/2011JPO4541.1.

Bertin, S., Rubio, A., Hernández-Carrasco, I., Solabarrieta, L., Ruiz, I., Sentchev, A., 2024. Coastal current convergence structures in the Bay of Biscay from optimized high-frequency radar and satellite data. Sci. Total Environ. 947, 174372. https://doi.org/10.1016/j.scitotenv.2024.174372).

Brando, V.E., Braga, F., Zaggia, L., Giardino, C., Bresciani, M., Matta, E., Carniel, S., 2015. High-resolution satellite turbidity and sea surface temperature observations of river plume interactions during a significant flood event. Ocean Sci. 11 (6), 909–920.

Chen, Z., Gong, W., Cai, H., Chen, Y., Zhang, H., 2017. Dispersal of the pearl river plume over continental shelf in summer. Estuar. Coast. Shelf Sci. 194, 252–262. https://doi.org/10.1016/j.ecss.2017.06.025.

Choi, J., Bracco, A., Barkan, R., Shchepetkin, A.F., McWilliams, J.C., Molemaker, J.M., 2017. Submesoscale dynamics in the northern Gulf of Mexico. Part III: Lagrangian implications. J. Phys. Oceanogr. 47 (9), 2361–2376. https://doi.org/10.1175/JPO-D-17-0036.1.

Cole, K.L., MacDonald, D.G., Kakoulaki, G., Hetland, R.D., 2020. River plume source-front connectivity. Ocean Model 150, 101571.

Coles, V.J., Brooks, M.T., Hopkins, J., Stukel, M.R., Yager, P.L., Hood, R.R., 2013. The pathways and properties of the Amazon River plume in the tropical North Atlantic Ocean. J. Geophys. Res. Ocean. 118, 6894–6913.

da Silva, C.E., Castelao, R.M., 2018. Mississippi River plume variability in the Gulf of Mexico from SMAP and MODIS-aqua observations. J. Geophy. Res.: Oceans 123, 6620–6638. https://doi.org/10.1029/2018JC014159.

Dagg, M., Benner, R., Lohrenz, S., Lawrence, D., 2004. Transformation of dissolved and particulate materials on continental shelves influenced by large rivers: plume processes. Cont. Shelf Res. 24 (7–8), 833–858. https://doi.org/10.1016/j.csr.2004.02.003.

Dai, A., Trenberth, K.E., 2002. Estimates of freshwater discharge from continents: latitudinal and seasonal variations. J. Hydrometeorol. 3 (6), 660–687. https://doi.org/10.1175/1525-7541(2002)003%3c0660:EOFDFC%3e2.0.CO.

D'Asaro, E.A., Shcherbina, A.Y., Klymak, J.M., Molemaker, J., Novelli, G., Guigand, C. M., Haza, A.C., Haus, B.K., Ryan, E.H., Jacobs, G.A., Huntley, H.S., Laxague, N.J.M., Chen, S., Judt, F., McWilliams, J.C., Barkan, R., Kirwan, A.D., Poje, A.C., Ozgökmen, T.M, 2018. Ocean convergence and the dispersion of flotsam. Proc. Natl. Acad. Sci. USA 115 (6), 1162–1167. https://doi.org/10.1073/PNAS.1718453115.

Do, H.T.T., Le, C.T., Bui, H.M., 2023. Assessing potential environmental exposure from chemical incidents in coastal Southeast Vietnam using remote sensing and mathematical modelling. Case Studies in Chemical and Environmental Eng 8, 100374. https://doi.org/10.1016/j.cscee.2023.100374.

d'Ovidio, F., Fernández, V., Hernández-García, E., Lopez, C., 2004. Mixing structures in the Mediterranean Sea from finite-size Lyapunov exponents. Geophys. Res. Lett. 31, L17203. https://doi.org/10.1029/2004GL020328.

d'Ovidio, F., Della Penna, A., Trull, T.W., Nencioli, F., Pujol, M.-I., Rio, M.-H., Park, Y.-H., Cotté, C., Zhou, M., Blain, S., 2015. The biogeochemical structuring role of horizontal stirring: Lagrangian perspectives on iron delivery downstream of the Kerguelen plateau. Biogeosciences 12, 5567–5581. https://doi.org/10.5194/bg-12-5567-2015.

D'Sa, E.J., Miller, R.L., McKee, B.A., 2007. Suspended particulate matter dynamics in coastal waters from ocean color: application to the northern Gulf of Mexico. Geophys. Res. Lett. 34 (23).

Enrile, F., Besio, G., Stocchino, A., Magaldi, M.G., 2019. Influence of initial conditions on absolute and relative dispersion in semi-enclosed basins. PLoS One 14, e0217073. https://doi.org/10.1371/journal.pone.0217073.

Foussard, A., Berti, S., Perrot, X., Lapeyre, G., 2017. Relative dispersion in generalized two-dimensional turbulence. J. Fluid Mech. 821, 358–383.

Garinet, A., Herrmann, M., Marsaleix, P., Pénicaud, J., 2024. Spurious numerical mixing under strong tidal forcing: a case study in the south-east Asian seas using the Symphonie model (v3. 1.2). Geosci. Model Dev. 17 (18), 6967–6986. https://doi.org/10.5194/gmd-17-6967-2024.

Gough, M.K., Reniers, A., Olascoaga, M.J., Haus, B.K., MacMahan, J., Paduan, J., Halle, C., 2016. Lagrangian coherent structures in a coastal upwelling environment. Cont. Shelf Res. 128, 36–50. https://doi.org/10.1016/j.csr.2016.09.007.

Han, A., Dai, M., Kao, S.J., Gan, J., Li, Q., Wang, L., Wang, L., 2012. Nutrient dynamics and biological consumption in a large continental shelf system under the influence of both a river plume and coastal upwelling. Limnol. Oceanogr. 57 (2), 486–502.

Hernández-Carrasco, I., L'opez, C., Hernández-García, E., Turiel, A., 2011. How reliable are finite-size Lyapunov exponents for the assessment of ocean dynamics? Ocean Model 36, 208–218. https://doi.org/10.1016/j.ocemod.2010.12.006.

Hernández-Carrasco, I., Orfila, A., Rossi, V., Garçon, V., 2018. Effect of small scale transport processes on phytoplankton distribution in coastal seas. Sci. Rep. 8, 8613. https://doi.org/10.1038/s41598-018-26857-9.

Hernández-Carrasco, I., Alou-Font, E., Dumont, P.A., Cabornero, A., Allen, J., Orfila, A., 2020. Lagrangian flow effects on phytoplankton abundance and composition along filament-like structures. Prog. Oceanogr. 189, 102469. https://doi.org/10.1016/j.pocean.2020.102469.

Hetland, R.D., Hsu, T.-J., 2013. Freshwater and sediment dispersal in large river plumes. In: Bianchi, T.S., Allison, M.A., Cai, W.-J. (Eds.), Biogeochemical Dynamics at Large River-Coastal Interfaces: Linkages With Global Climate Change. Springer, New York, pp. 55–85. https://doi.org/10.1017/CBO9781139136853.

Horner-Devine, A.R., Jay, D.A., Orton, P.M., Spahn, E.Y., 2009. A conceptual model of the strongly tidal Columbia River plume. J. Mar. Syst. 78, 460–475. https://doi.org/10.1016/j.jmarsys.2008.11.025.

Horner-Devine, A.R., Hetland, R.D., MacDonald, D.G., 2015. Mixing and transport in coastal river plumes. Annu. Rev. Fluid Mech. 47 (1), 569–594. https://doi.org/10.1146/annurev-fluid-010313-141408.

Huntley, H.S., Lipphardt Jr., B.L., Kirwan Jr., A.D., 2011. Surface Drift Predictions of the Deepwater Horizon Spill: The Lagrangian Perspective. In: Macfadyen, A., Ji, Z.-G., Weisberg, R.H. (Eds.), Monitoring and Modeling the Deepwater Horizon Oil Spill. Geophysical Monograph Series, Wiley. https://doi.org/10.1029/2011GM001097.

Jay, D.A., Pan, J., Orton, P.M., Horner-Devine, A.R., 2009. Asymmetry of tidal plume fronts in an eastern boundary current regime. J. Mar. Syst. 78, 442–459.

Jay, D.A., Zaron, E.D., Pan, J., 2010. Initial expansion of the Columbia River tidal plume: theory and remote sensing observations. J. Geophys. Res. 115, C00B15.

Jones, C.E., Dagestad, K.F., Breivik, Ø., Holt, B., Röhrs, J., Christensen, K.H., Skrunes, S., 2016. Measurement and modeling of oil slick transport. J. Geophys. Res. Oceans 121 (10), 7759–7775.

Kubryakov, A., Stanichny, S., Zatsepin, A., 2016. River plume dynamics in the Kara Sea from altimetry-based lagrangian model, satellite salinity and chlorophyll data. Remote Sens. Environ. 176, 177–187. https://doi.org/10.1016/j.rse.2016.01.020.

LaCasce, J.H., 2008. Statistics from Lagrangian observations. Prog. Oceanogr. 77, 1–29.

Large, W.G., Yeager, S., 2004. Diurnal to Decadal Global Forcing for Ocean and Sea–Ice Models: The Data Sets and Flux Climatologies, NCAR Technical Note, NCAR/TN-460+STR. National Center for Atmospheric Research, Boulder, CO. https://doi.org/10.5065/D6KK98Q6.

Lyard, F.H., Allain, D.J., Cancet, M., Carrère, L., Picot, N., 2021. FES2014 global ocean tide atlas: design and performance. Ocean Sci. 17 (3), 615–649. https://doi.org/10.5194/os-17-615-2021.

MacCready, P., Banas, N.S., Hickey, B.M., Dever, E.P., Liu, Y., 2009. A model study of tide- and wind-induced mixing in the Columbia River estuary and plume. Cont. Shelf Res. 29, 278–291.

Marmorino, G.O., Trump, C.L., 2000. Gravity current structure of the Chesapeake Bay outflow plume. J. Geophys. Res. 105, 28847–28861. https://doi.org/10.1029/2000JC000225.

Marsaleix, P., Auclair, F., Floor, J.W., Herrmann, M.J., Estournel, C., Pairaud, I., et al., 2008. Energy conservation issues in sigma–coordinate free–surface ocean models. Ocean Model 20, 61–89. https://doi.org/10.1016/j.ocemod.2007.07.005.

Moline, M.A., Frazer, T.K., Chant, R., Glenn, S., Jacoby, C.A., Reinfelder, J.R., Schofield, O., 2008. Biological responses in a dynamic buoyant river plume. Oceanography 21 (4), 70–89.

Morozov, E.G., Frey, D.I., Salyuk, P.A., Budyansky, M.V., 2024. Amazon River plume in the Western tropical North Atlantic. J Mar Sci Eng 12, 851. https://doi.org/10.3390/jmse12060851.

Nash, J.D., Kilcher, L.F., Moum, J.N., 2009. Structure and composition of a strongly stratified, tidally pulsed river plume. J. Geophys. Res. 114, 42. https://doi.org/10.1029/2008JC005036.

Neumann, L.E., Šim°unek, J, Cook, F.J., 2011. Implementation of quadratic upstream interpolation schemes for solute transport into HYDRUS–1D. Environ. Model Softw. 26, 11. https://doi.org/10.1016/j.envsoft.2011.05.010.

Nguyen-Duy, T., Ayoub, N.K., Marsaleix, P., Toublanc, F., De Mey-Frémaux, P., Piton, V., Ngo-Duc, T., 2021. Variability of the Red River plume in the Gulf of Tonkin as revealed by numerical modeling and clustering analysis. Front. Mar. Sci. 8, 77213. https://doi.org/10.3389/fmars.2021.772139.

Nguyen-Duy, T., Ayoub, N.K., De-Mey-Frémaux, P., Ngo-Duc, T., 2023. How sensitive is a simulated river plume to uncertainties in wind forcing? A case study for the Red River plume (Vietnam). Ocean Model 186, 102256.

O'Donnell, J., 2010. The dynamics of estuary plumes and fronts. In: Valle Levinson, A. (Ed.), Contemporary Issues in Estuarine Physics. Cambridge Univ. Press, Cambridge, pp. 186–246. https://doi.org/10.1017/CBO9780511676567.

O'Donnell, J., Marmorino, G.O., Trump, C.L., 1998. Convergence and downwelling at a river plume front. J. Phys. Oceanogr. 28 (7), 1481–1495. https://doi.org/10.1175/1520-04851998028.

Ohlmann, J.C., Romero, L., Pallàs-Sanz, E., Perez-Brunius, P., 2019. Anisotropy in coastal ocean relative dispersion observations. Geophys. Res. Lett. 46 (2), 879–888. https://doi.org/10.1029/2018GL081186.

Orton, P.M., Jay, D.A., 2005. Observations at the tidal plume front of a high-volume river outflow. Geophys. Res. Lett. 32:L11605. Doi: 10.1029/2005GL022372Jay, David a., Jiayi Pan, Philip M. Orton, and Alexander R. Horner-Devine. "asymmetry of Columbia River tidal plume fronts.". J. Mar. Syst. 3 (2009), 442–459.

Piton, V., Herrmann, M., Marsaleix, P., Duhaut, T., Ngoc, T.B., Tran, M.C., Shearman, K., Ouillon, S., 2021. Influence of winds, geostrophy and typhoons on the seasonal variability of the circulation in the Gulf of Tonkin: a high–resolution 3D regional modeling study. Reg. Stud. Mar. Sci. 45, 101849. https://doi.org/10.1016/j.rsma.2021.101849.

Rogowski, P., Zavala-Garay, J., Shearman, K., Terrill, E., Wilkin, J., Tran, H.L., 2019. Air-sea-land forcing in the Gulf of Tonkin: assessing seasonal variability using modern tools. Oceanography 32, 150–161. https://doi.org/10.5670/oceanog.2019.223.

Schroeder, T., Devlin, M.J., Brando, V.E., Dekker, A.G., Brodie, J.E., Clementson, L.A., McKinna, L., 2012. Inter-annual variability of wet season freshwater plume extent into the great barrier reef lagoon based on satellite coastal ocean colour observations. Mar. Pollut. Bull. 65, 210–223. https://doi.org/10.1016/j.marpolbul.2012.02.022.

Stashchuk, N., Vlasenko, V., 2009. Generation of internal waves by a supercritical stratified plume. J. Geophys. Res. Oceans 114 (C1).

Taylor, G.I., 1922. Diffusion by continuous movements. Proc. Lond. Math. Soc. 2, 196–212.

Thomson, R.E., Emery, W.J., 2014. Data Analysis Methods in Physical Oceanography. Elsevier. ISBN 978–0–12-387782-6.

Toublanc, F., Ayoub, N.K., Marsaleix, P., 2023. On the role of wind and tides in shaping the Gironde River plume (Bay of Biscay). Cont. Shelf Res. 253. https://doi.org/10.1016/j.csr.2022.104891.

Tran, M.C., Sentchev, A., Nguyen, K.C., 2021. Multi-scale variability of circulation in the Gulf of Tonkin from remote sensing of surface currents by high-frequency radars. Ocean Dyn. 71, 175–194. https://doi.org/10.1007/s10236-020-01440-x.

Tran, M.C., Sentchev, A., Berti, S., Ayoub, N.K., Nguyen-Duy, T., Cuong, N.K., 2022. Assessment of relative dispersion in the Gulf of Tonkin using numerical modeling and HF radar observations of surface currents. Cont. Shelf Res. 245, 104784.

Vinh, V.D., Ouillon, S., Thanh, T.D., Chu, L.V., 2014. Impact of the Hoa Binh dam (Vietnam) on water and sediment budgets in the Red River basin and delta. Hydrol. Earth Syst. Sci. 18, 3987–4005.

Vlasenko, V., Stashchuk, N., McEwan, R., 2013. High-resolution modelling of a large-scale river plume. Ocean Dyn. 63 (11), 1307–1320.

Warrick, J.A., Farnsworth, K.L., 2017. Coastal river plumes: collisions and coalescence. Prog. Oceanogr. 151, 245–260.

Whitney, M.M., Jia, Y., Cole, K.L., MacDonald, D.G., Huguenard, K.D., 2021. Freshwater composition and connectivity of the Connecticut River plume during ambient flood tides. Front. Mar. Sci. 8, 747191. https://doi.org/10.3389/fmars.2021.747191.

Yankovsky, A.E., Fribance, D.B., Cahl, D., Voulgaris, G., 2022. Offshore spreading of a supercritical plume under upwelling wind forcing: a case study of the Winyah Bay outflow. Front. Mar. Sci. 8, 785967. https://doi.org/10.3389/fmars.2021.785967.

Yaremchuk, M., Sentchev, A., 2009. Mapping radar-derived sea surface currents with a variational method. Cont. Shelf Res. 29 (14), 1711–1722.